Massive-scale spatial multiplexing of multimode VCSELs with a 3D-printed photonic lantern: Supplementary

IL estimator serving as a lower bound of the actual IL

In the design of a multimode PL, we use an IL estimator defined by

$$\hat{IL} = \frac{1}{N} \sum_{i=1}^{S} M_i \cdot P_i \leq 1, \tag{1}$$

where:

- N is the total number of output modes (e.g., 42, 114, or 222),
- S is the number of symmetry groups (2, 3, or 4 for 7-, 19-, or 37-MM PLs),
- M_i is the number of modes in the i-th symmetry group (number of sources times 6 modes in each source) , with $\sum_{i=1}^{S} M_i = N$,
- P_i is the power transmitted from the highest-order mode of a representative source in the i-th symmetry group to all output modes, computed via a single FDTD simulation.

The IL estimator is always less than or equal to the real IL calculated from the transfer matrix (TM) singular values. This result stems from the estimator's reliance on the highest-order input modes, which are the lossiest due to their high transverse momentum and lowest effective refractive index, as outlined in the PL design methodology. Below, we provide a detailed explanation grounded in SVD and matrix normalization.

Transfer Matrix and Frobenius Norm

The TM A is an $m \times n$ complex matrix, where m is the number of output modes (e.g., 42, 114, or 222 for 7-, 19-, or 37-MM PLs) and n is the number of input modes (e.g., $7 \times 6 = 42$, $19 \times 6 = 114$, or $37 \times 6 = 222$, accounting for 6 modes per source). The Frobenius norm squared,

$$\|A\|_F^2 = \sum_{i=1}^{m} \sum_{j=1}^{n} |a_{ij}|^2, \tag{2}$$

where a_{ij} are the TM elements, represents the total power transferred from all input modes to all output modes, assuming each input mode is normalized (unit power). Via SVD, $A = U\Sigma V^{\dagger}$, where Σ contains the singular values $\sigma_1 \geq \sigma_2 \geq \cdots \geq \sigma_p \geq 0$ (where $p = min(m,n)$), and

$$\|A\|_F^2 = \sum_{i=1}^{p} \sigma_i^2. \tag{3}$$

For a lossless (unitary) PL, $A^{\dagger}A = I$, all $\sigma_i = 1$, and $\|A\|_F^2 = n$. In practice, losses reduce the Frobenius norm $\|A\|_F^2 \leq n$. Normalizing by the number of output modes m (typically $m \geq n$), we get:

$$\frac{\|A\|_F^2}{m} \leq \frac{n}{m} \leq 1. \tag{4}$$

IL Estimator

Observing equation (1), each $P_i = \sum_{k=1}^{m} |a_{k,j_i}|^2$, where j_i indexes the highest-order mode's column in A, assuming unit input power. Thus:

$$\hat{IL} = \frac{1}{N} \sum_{i=1}^{S} M_i \cdot \|\mathbf{a}_{j_i}\|^2, \tag{5}$$

where $\mathbf{a}_{j_i}$ is the j_i-th column of A.

Highest-Order Modes Are Lossiest

The estimator uses the highest-order modes because they have the highest transverse momentum and the lowest effective index, making them the most challenging to couple adiabatically into the output waveguide. Consequently, their power transmission, $\|\mathbf{a}_{j_i}\|^2$, is less than or equal to that of lower-order modes, $\|\mathbf{a}_j\|^2$, which couple more efficiently. This behavior has been demonstrated empirically through simulations. The Frobenius norm, however, accounts for all input modes:

$$\|A\|_F^2 = \sum_{j=1}^{n} \|\mathbf{a}_j\|^2. \tag{6}$$

Since the estimator samples only the lossiest modes:

$$\sum_{i=1}^{S} M_i \cdot \|\mathbf{a}_{j_i}\|^2 \leq \sum_{j=1}^{n} \|\mathbf{a}_j\|^2, \tag{7}$$

because $\|\mathbf{a}_{j_i}\|^2 \leq \|\mathbf{a}_j\|^2$ for lower-order modes j.

Comparison

Normalizing by N:

$$\hat{IL} = \frac{1}{N} \sum_{i=1}^{S} M_i \cdot \|\mathbf{a}_{j_i}\|^2, \quad \frac{\|A\|_F^2}{N} = \frac{1}{N} \sum_{j=1}^{n} \|\mathbf{a}_j\|^2. \tag{8}$$

Since the estimator's sum involves only the lossiest modes' columns, while $\|A\|_F^2$ includes all modes (many with higher power transmission), we have:

$$\hat{IL} \leq \frac{\|A\|_F^2}{N} = \frac{1}{N} \sum_{i=1}^{p} \sigma_i^2 = IL. \tag{9}$$

where σ_i are the TM singular vlaues. We see that the real IL which is the average of the singular values squared is equal or larger than the IL estimator.

Spatial mode generation setup

Implementing the transfer matrix measurement described in the manuscript requires the efficient generation of 42 LP fiber modes. A common approach for mode conversion utilizes a single plane with phase-only modulation. In this technique, the phase distribution of the input beam is modulated by a phase modulation designed to match the phase profile of the target mode. However, the modulated beam inevitably includes components of various unintended modes, as the phase plate can only manipulate the phase distribution, not the full complex amplitude. When the number of modes in the system is small, this issue is minimal, as most unwanted modes radiate from the fiber. However, as the number of multiplexed modes increases, these additional components contribute to modal crosstalk [1]. To achieve high phase conjugation fidelity, a wavefront modulation method must support full complex modulation with a resolution comparable to that of the phase mask. Unfortunately, this level of control cannot be achieved with a single phase mask[2]. Therefore, we utilize a dual phase mask method for this mode conversion task. The Spatial Light Modulator (SLM) was devided to two halves where each is a single phase mask (Figure.1-c).

The algorithm for generating phase holograms to convert a Gaussian laser beam into a specific mode pattern is based on gradient descent. The SLM pixels act as optimization variables, and in each iteration, the algorithm updates these variables in the direction of the gradient vector of the merit function with respect to the SLM pixels. To implement this, we developed a simulation model of the mode conversion system (Figure.1-a).

The simulation begins with an input Gaussian beam, E_{in}, assumed to be collimated (flat phase front). The beam passes through the first phase mask, Φ_1, corresponding to the first strike on the SLM, resulting in the field E_1. It then propagates over a distance Z_1, representing the separation between the SLM and the mirror, to the second half of the SLM, resulting in E_2. After transmission through the second phase mask, Φ_2, the field becomes E_3. Subsequently, the beam undergoes free-space propagation over a distance Z_2, leading to E_4, followed by propagation through a lens. Finally, E_{out} represents the field at the focal plane of the lens. We will describe the field evolution throughout the system in a mathematical form. The angular spectrum method is used for free-space propagation. Below are the notations:

1. FFT - Fast Fourier Transform.
2. $H(z) = \exp\left(jz\sqrt{\left(\frac{2\pi}{\lambda}\right)^2 - (k_x^2 + k_y^2)}\right)$ - Angular spectrum free-space propagation kernel, where $k_{x/y}$ are the spatial frequencies in the simulation region.
3. $h(f) = \exp\left(-j\frac{2\pi}{\lambda}\frac{x^2+y^2}{2f}\right)$ - Lens kernel with focal length f.
4. $\Phi_{1/2}$ - The first and second phase masks.

We will define a forward function $\mathscr{F}$ that takes E_{in} as input and returns E_{out}. The steps of the algorithm are as follows:

1. **Input Field Initialization** Define the input Gaussian beam:

   $E_{\text{in}} = \text{Input field}$

2. **Apply First Phase Mask** Multiply the input field by the first phase mask:

   $E_1 = E_{\text{in}} \cdot \exp(j\Phi_1)$

3. **Free-Space Propagation to Mirror** Propagate E_1 through a distance Z_1:

   $E_2 = \text{FFT}^{-1}\left(\text{FFT}(E_1) \cdot H(Z_1)\right)$

4. **Apply Second Phase Mask** Multiply the field by the second phase mask:

   $E_3 = E_2 \cdot \exp(j\Phi_2)$

5. **Free-Space Propagation to Lens** Propagate E_3 through a distance Z_2:

   $E_4 = \text{FFT}^{-1}\left(\text{FFT}(E_3) \cdot H(Z_2)\right)$

6. **Lens Transformation and propagation to the focal plane** Apply the lens kernel and f distance propagation:

   $E_{\text{out}} = FFT^-1(FFT(E_4 \cdot h(f)) \cdot H(f))$

7. **Output Field** Return E_{out} as the result of the forward function $\mathscr{F}$.

Next, we define the merit function to optimize. Our objective is to convert the field into a specific target mode distribution. Therefore, the immediate optimization goal is to maximize the complex overlap integral between the resulting field, E_{out}, and the target mode, E_{target}. This can be expressed as:

$$\eta = |\langle E_{\text{out}} | E_{\text{target}} \rangle|^2 = |\langle \mathscr{F}(E_{\text{in}}) | E_{\text{target}} \rangle|^2 \tag{10}$$

While numerical results are excellent, practical considerations must be addressed. One such consideration is the smoothness of the phase mask. High-frequency changes between phase elements on the SLM may not significantly affect the optical beam or can cause scattered light. To mitigate this, a total variation (TV) function is added as a regularization term to the optimization function [3].

The revised optimization function becomes:

$$\mathscr{L} = -(|\langle \mathscr{F}(E_{\text{in}}) | E_{\text{target}} \rangle|^2 + \lambda_1 \cdot TV(\Phi_1, \Phi_2)) \tag{11}$$

where λ_1 is a constant (ranging from 0 to 1) that determines the smoothness of the phase masks. A higher λ_1 increases smoothness but reduces coupling efficiency. The negative sign is a technical implementation detail of minimizing the function, but the same approach can be adapted for gradient ascent as well. Based on empirical experimentation, $\lambda_1 = 10^{-5}$ was selected. Another important consideration is the practical mismatch between the simulated environment and the optical setup. It is essential to align the simulated dimensions—such as SLM pixel size, beam size, propagation distances, and lens focal

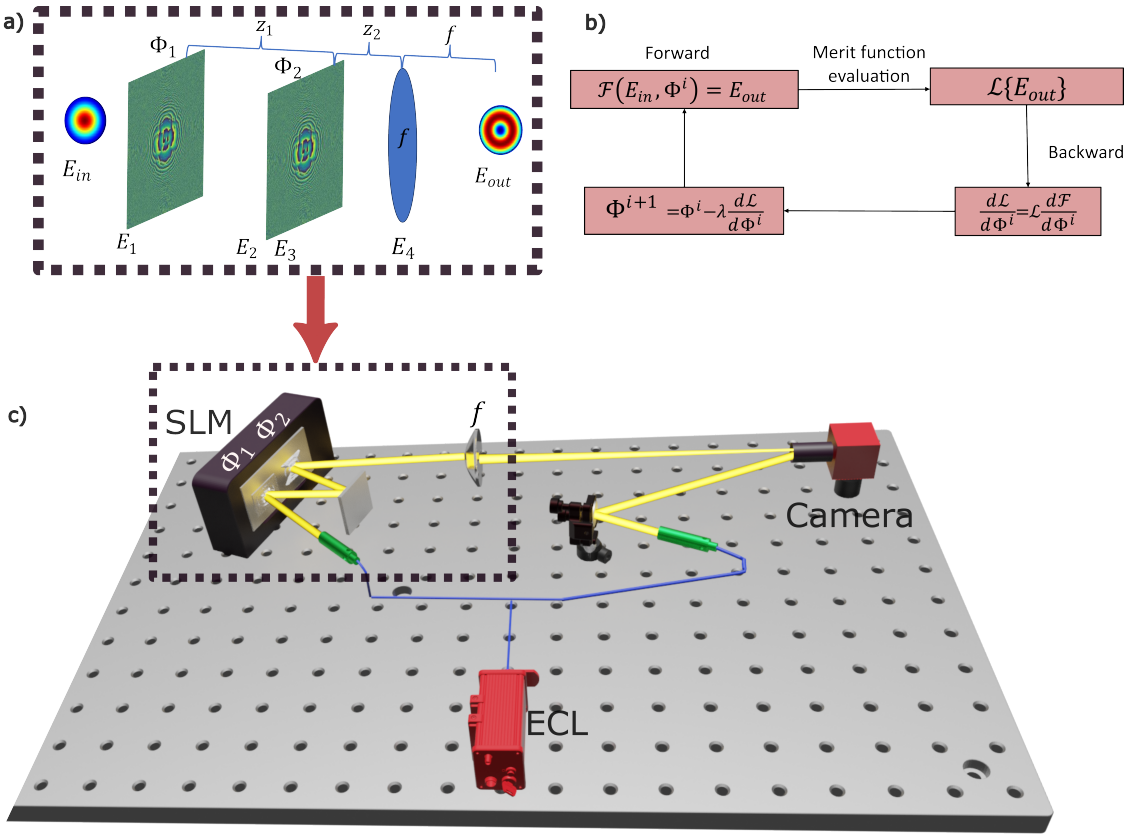

Figure 1. a) Schematic of the simulated system. b) Gradient descent optimization flow: Φ^i; The phase masks optimization parameter,λ-Learning rate of the gradient descent. $\mathscr{L}$; Loss function, $\mathscr{F}$ forward function. c) Experimental set-up schematic.

lengths—with the experimental setup to ensure the method's effectiveness. However, alignment issues, tilting elements, and optical aberrations can introduce mismatches that result in losses in mode coupling efficiency.

To implement the gradient descent optimization, we utilized PyTorch Autodiff, an automatic differentiation library in Python primarily used for training neural networks. This library enables the calculation of derivatives of the merit function $\mathscr{L}$ with respect to the phase mask pixels [4]. The gradient descent loop is illustrated in Figure.1-b.

Figure.2-a shows the resulting fields measured using digital holography, with the experimental setup illustrated in Figure.1-c. Figure.2-b depicts the algorithm's evolution for all mode cases, demonstrating rapid convergence after only 120 iterations. Figure.2-c presents the coupling efficiency, or modal purity, of the generated modes, with values exceeding -0.75 dB. Figure.2-d displays the results of an orthogonality test for the generated modal basis. The off-diagonal elements are below -20 dB, indicating low crosstalk between modes, a critical parameter for transfer matrix measurements.

VCSEL source Beam quality and modal content measurements

Before measuring the PL we measured the emission from a single VCSEL source (electric fields) at different injection currents (4.3 mA to 11mA normlized per VCSEL source) and performed modal decomposition for each measurement. During the printing process, the VCSEL cavity is filled with photopolymer, which can affect the lasing conditions and modes. To ensure accurate measurement, the analysis was performed on a VCSEL with a 3D-printed pillar that completely filled the aperture. This approach ensures that the measured field closely aligns with the field entering the PL waveguides. Figure.3-a displays the VCSEL's electric field , along with its modal content and M^2 at different currents. As expected, higher currents excite higher-order modes, leading to an increase in M^2 (Figure.3-b). Most of the power is concentrated in the first six LG modes, with a small fraction extending up to the 12th mode at higher currents. The M^2 varies between 2.25 and 4.1.

Since the PL multiplexes multiple sources into a single waveguide, the PL's output combines the spectral information of all the coupled sources. In self-interference holographic measurements, which rely on a spatially filtered signal as the reference, it is crucial to evaluate whether the spectral information remains highly correlated with the original signals. This is because each source interferes with itself, and each carries slightly distinct spectral characteristics.

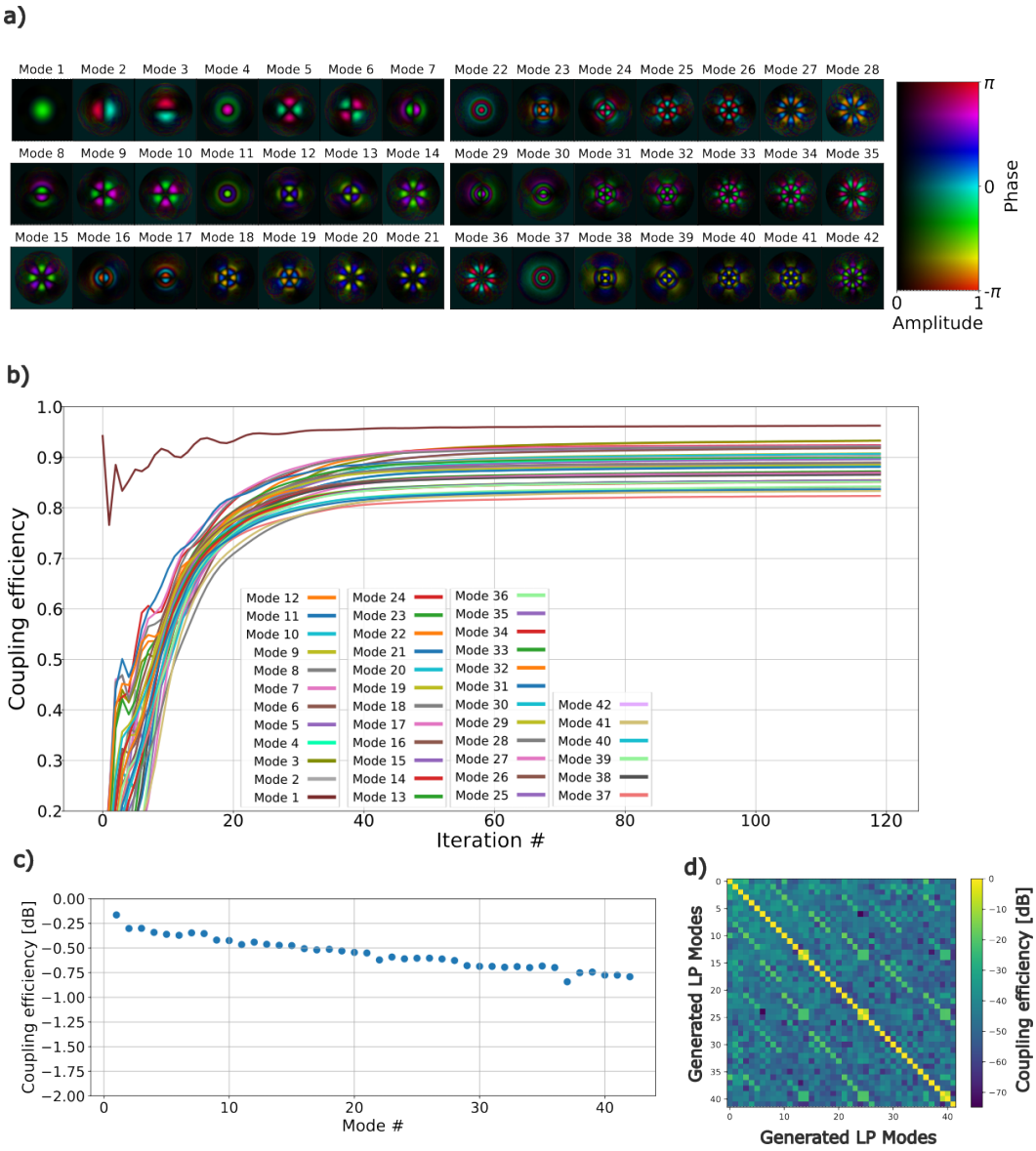

Figure 2. a) Visualization of the 42 generated fields. b) Mode purity evolution across algorithm iterations for each mode. c) Final mode purity achieved for each mode at the conclusion of the algorithm. d) Orthogonality of the generated modes.

To investigate this, we measured the spectra of the light emerging from the 37-mode photonic lantern and the spatially filtered reference beam using an Optical Spectrum Analyzer (OSA). Figure 4 illustrates the spectral measurements at various injection currents. Each plot presents the spectra of both signals (blue and black curves) in dB scale, along with the ratio (in dB) between the two curves (red curve). Across all measurements, the total power decreased by a factor of approximately 25 to 30.

To quantify the similarity between the spectral curves, we computed the normalized cross-correlation function. In all cases, the correlation values exceeded 94%, demonstrating a very high level of similarity. Since each source operates as its own coherent detection oscillator, it is vital to verify whether the ratio between the two spectra remains stable across the relevant wavelength range. Variations in this ratio could cause apodization during the holography process, potentially affecting the accuracy of the reconstructed field.

As depicted in Fig. 4, the ratio curve remains flat over a wavelength range encompassing 95% of the spectral power. This confirms the stability of the spectral relationship and ensures negligible impact on the holographic process.

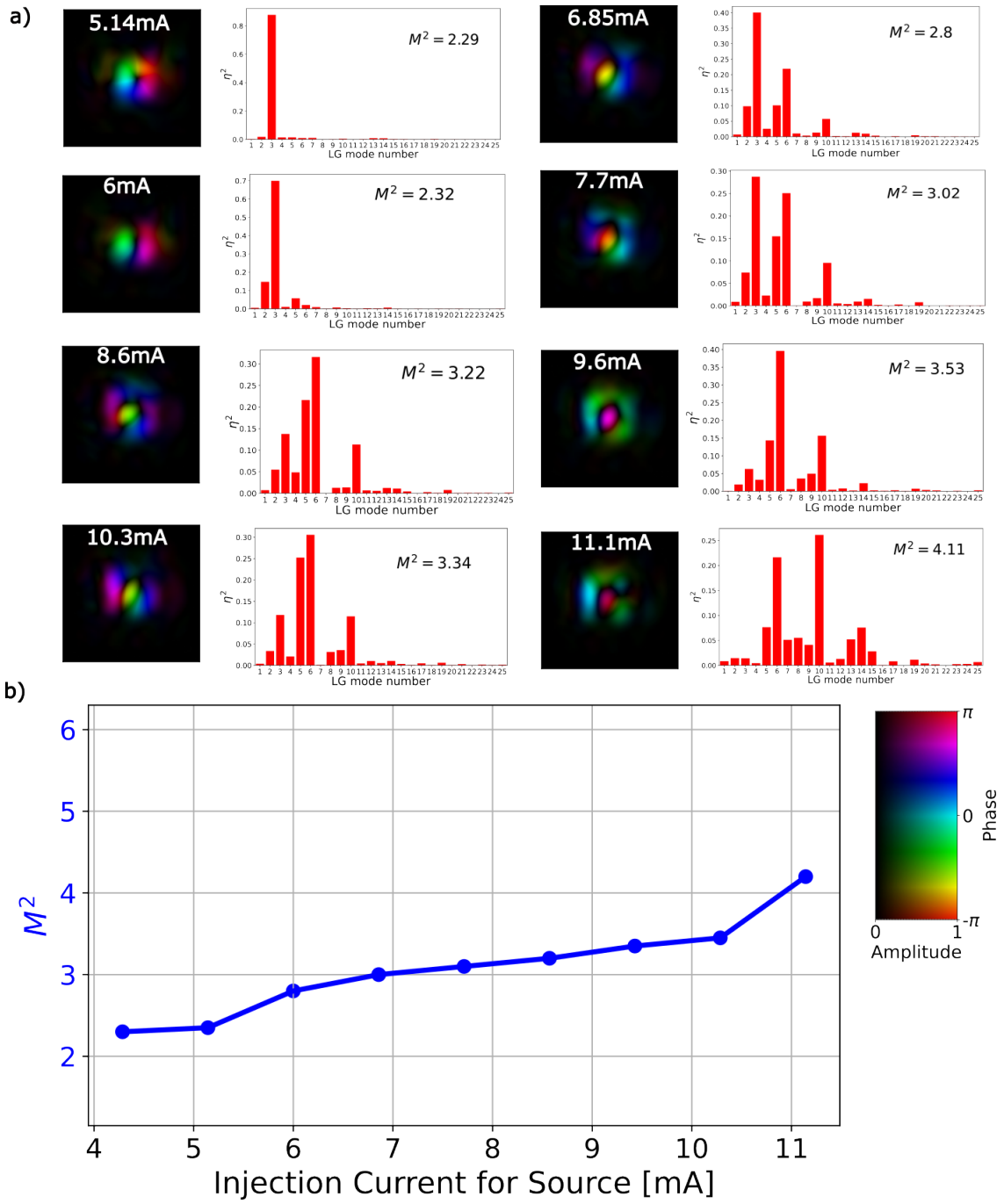

Figure 3. a) Measured complex field and modal distribution of a single VCSEL source at different currents. b) Measured M^2 vs different currents per VCSEL source (4.3–11.2 mA).

Lens System simulation

To assess the performance of an imaging system for incoherent beam combining and fiber coupling, we conducted a numerical simulation of the system. The setup, depicted in Figure.5-a, consists of an incoherent array of sources, a microlens array (MLA) for collimating the independent sources, a focusing lens, and a multimode fiber (MMF) positioned at the lens's focal plane. Numerical simulations were performed using Python and the Angular Spectrum algorithm for physical optics propagation [5].

In the simulation, each VCSEL source was modeled independently, and its fiber coupling efficiency was calculated. The simulation focused on multiplexing 37 sources arranged in a triangular grid with a pitch of 44 μm. The grid arrangement is shown in Figure.5-b. The sources were categorized into six unique groups based on their distance from the central source,

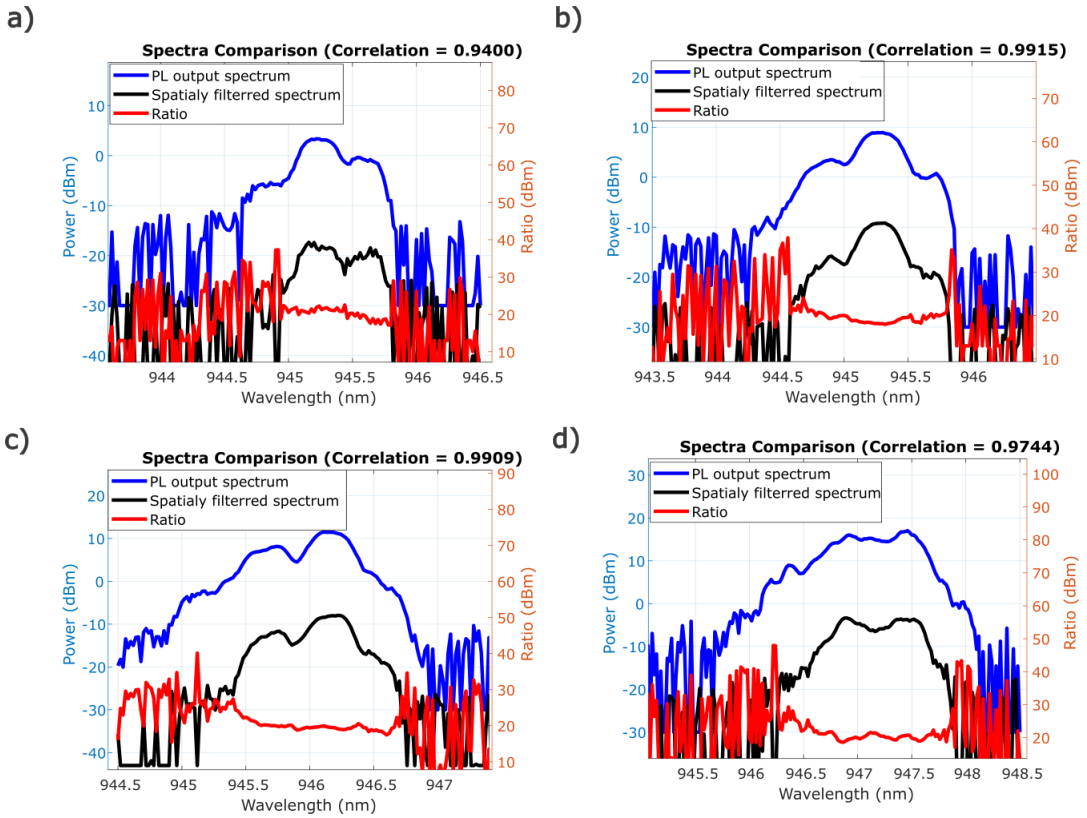

Figure 4. Spectrum comparison between spatially filtered and non filtered PL output at injection current per VCSEL of a) 6.1 mA, b) 8.1 mA, c) 10.2 mA and d) 12.2 mA.

labeled "A" to "F." Table.1 lists the distances and multiplicities of each source group. Due to the symmetry of the grid, only six simulations were required instead of 37.

Each source was treated as capable of supporting six Laguerre-Gaussian (LG) modes of equal power. To simulate the modal behavior, each mode was launched separately, and its coupling efficiency was calculated after propagating through the system. Consequently, the coupling efficiency of the entire array was determined using $6\,(\textbf{Modes} \times 6\,\textbf{Groups})$ simulations. The fiber coupling efficiency was computed as:

$$\eta_T = \frac{1}{N}\sum_{i=1}^{N} M_i \cdot \sum_{i,j=1}^{6} \frac{\eta_{i,j}}{6} \tag{12}$$

Here, N represents the total number of sources (37), M_i denotes the number of duplications in the i-th group (e.g., for group "B," $M = 6$), and $\eta_{i,j}$ is the coupling efficiency when launching the j-th mode from the i-th source location. This formula provides a weighted average of the coupling efficiency across all possible cases.

In the system we used a $50\mu m$ diameter core fiber with NA=0.12 which is supporting approximatly $37 \times 6 = 222$ ($V = 21.1$, $V^2/2 = 222.6$) guided modes. As a source we used LG beams with $MFD = 10\mu m$ for the fundamental mode. The source is simulating the VCSEL array we are using in this work. The system has two degreess of freedom to optimize which are the focal length for the two lenses. In addition to finding the fibers' acceptable multimode beam sizes for efficient coupling, when we deal with VCSELs placed in array form then the collimating lenses' finite apertures may clip beam contents extending beyond their diameter. The MLA lens apertures can be as large as the VCSEL source pitch, and no further. What we can control is the beam size within the beam aperture. If we underfill the aperture, meaning the beam size is much smaller than the aperture, then the aperture throughput will be very high (or low clipping). However, small beams do not couple efficiently to the fiber, as we previously saw. Conversely, if we overfill the aperture, meaning the beam size is larger than the aperture, then the aperture throughput will be low (due to clipping). However, the remaining beam transmitting through the aperture will likely efficiently couple to the fiber. This suggests that a system optimization needs to be performed. We assess here the beam clipping impact by measuring the aperture throughput as a function of the beam size with respect to the aperture size. This clipping will also be mode dependent, as higher order modes extend further out making them more prone to clipping loss.

Group	Distance	Duplication
"A"	0	1
"B"	$1 \times$ **Pitch**	6
"C"	$\sqrt{3} \times$ **Pitch**	6
"D"	$2 \times$ **Pitch**	6
"E"	$\sqrt{7} \times$ **Pitch**	12
"F"	$3 \times$ **Pitch**	6

Table 1. Identification of unique groups of VCSELs experiencing identical fiber coupling due to being equally placed in radial distance.

To optimize the system, we varied the focal lengths of both lenses and evaluated the results, as shown in Figure.5. The coupling efficiency is plotted for different numbers of sources being coupled to the fiber. Notably, for a small number of sources (1 and 7), the efficiency remains very high (Figure.5-c,d), exceeding 0.3 dB. However, when attempting to couple 37 sources (Figure.5-f), corresponding to matching the number of source modes to the number of fiber modes, the efficiency drops significantly.

VCSEL Integration and 3D-Printing Process Flow

The multimode VCSEL sources used in our reported photonic lantern (PL) multiplexing work utilized a commercially available chip produced by VIXAR, model V00132, containing approximately 1700 sources on a triangular grid (pitch of 44 μm), operated in parallel by a single injection current drive source. The chip (see Fig. 6) measures approximately 2 $\times$ 2 mm, with the laser sources occupying the central 1.7 $\times$ 1.7 mm active zone. The surrounding periphery region serves as a common anode available for wire bonding, while the bottom surface serves as the cathode.

We developed a custom process flow compatible with our 3D-printing workflow directly onto the VCSEL chips, including chip assembly, singulation to smaller emitter arrays, and printing. The PL input counts demonstrated (7, 19, and 37), ultimately limited by the transverse writing range of the Nanoscribe printer, are two orders of magnitude smaller than the number of sources on the VIXAR chip. Hence, we singulate smaller arrays to match the VCSEL count needed for a PL implementation, reducing drive current, conserving activation power, lowering thermal load, and enabling multiple independently operable PLs on the same chip.

Singulation is achieved via 50 μm deep trenches into the chip using a high-precision dicing saw, which cuts through the top gold conductive layer and underlying semiconductor layers. Since the chip is only 100 μm thick, such trenches make it prone to fracture. To mitigate this, the VCSEL chip is first soldered onto a Beryllium Oxide (BeO) submount (13 $\times$ 5 mm $\times$ 15 mil) featuring a gold-coated surface and centrally deposited eutectic AuSn solder for cathode contact. Soldering is performed in a clean room using a Semiconductor Equipment Corp. Eagle 860 bonder, which aligns the chip to the submount and uniformly raises their temperatures just above the 280°C solder melting point, resulting in a soldered chip (see Fig. 6).

Before dicing, the VCSEL front facet is coated with a thin photoresist layer to prevent particle contamination, especially inside the cavities. The chip and submount are mounted on dicing tape and diced (ADT Provectus 7100) using a diamond blade at 20,000 RPM with water coolant. Four dicing streets (50 μm deep) define the four singulated corners, each matched to the target PL array size (see Fig. 6).

After dicing, the photoresist is removed using acetone and ultrasonic cleaning. The BeO-mounted VCSEL is then soldered onto a custom copper-core PCB (instead of FR4) for improved thermal performance. The PCB includes thermistor placement and a flat cable connector. Wire bonds connect each of the four VCSEL corner peripheries to corresponding contact pads on the PCB at a substrate temperature of 130°C (see Fig. 6).

We chose to wire bond before 3D printing to avoid collision between the bonding needle and printed PLs. However, this constrains the wire loop height to below the Nanoscribe's objective working distance (380 μm), thus limited to 300 μm. Wire bonds are also applied away from VCSEL apertures to avoid obstruction of the high-NA laser beam. Fig. 6 shows the VIXAR chip with wire bonds.

The VCSEL chip, mounted and wire bonded, allows individual lasing of each corner via current injection. Fig. 6 shows lasing from one corner (captured with a CMOS camera sensitive to 940 nm). Also visible are grounding wires connecting the submount top surface to the PCB ground pad (four wires to reduce current density if all corners lase simultaneously).

A drop of IP-S photopolymer is then cast on the die with a syringe for dose control. The PCB-mounted chip is placed in a custom holder with spring-like flexure beams for stable positioning during printing. The holder is inserted into the Nanoscribe system, where the chip is leveled and aligned. Anchor points on the die are selected for alignment.

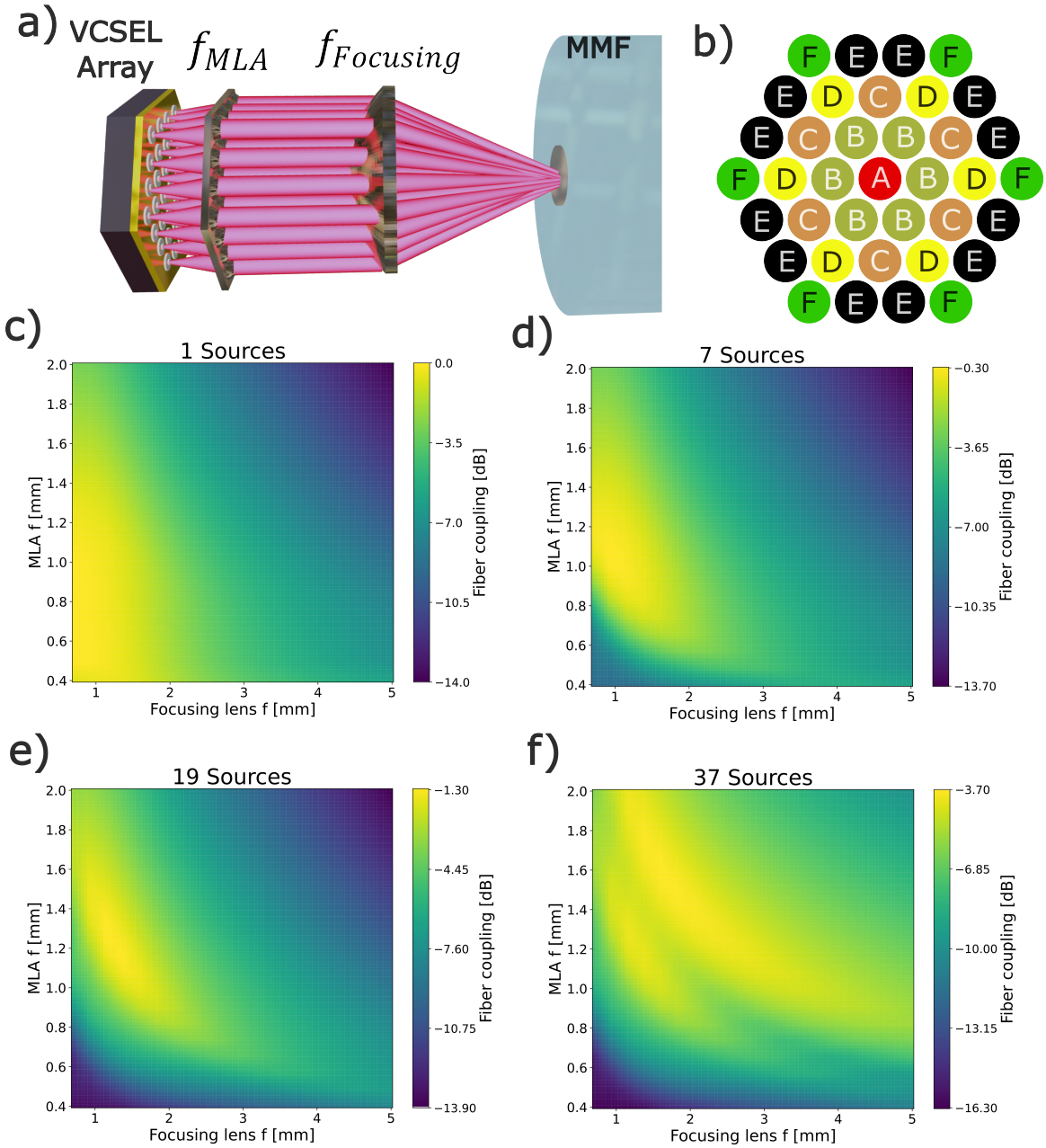

Figure 5. a) Schematic of the simulated system. b) Triangular grid arrangement of VCSELs participating in the coupling study, with 37 sources grouped and labeled as A, B, C, D, E, and F. Fiber coupling efficiency as a function of MLA focal length and focusing lens focal length is shown for: c) a single VCSEL source, d) 7 VCSEL sources, e) 19 VCSEL sources, and f) 37 VCSEL sources.

We found improved registration when aligning the model to the active lasing mode rather than to the physical apertures. Hence, we perform active alignment by turning on the VCSELs and marking beam centroids as alignment anchors using the Nanoscribe microscope camera (which is sensitive to 940 nm).

Printing then begins with optimized parameters (laser power, scan speed, hatching/slicing distances). Post-printing, the PCB is immersed in PGMEA for 20 minutes, rinsed with IPA, and dried with Novec fluid. At this stage, the VCSEL printing is complete, and lab testing may proceed. SEM images of printed PLs appear in the main manuscript (Fig. 2).

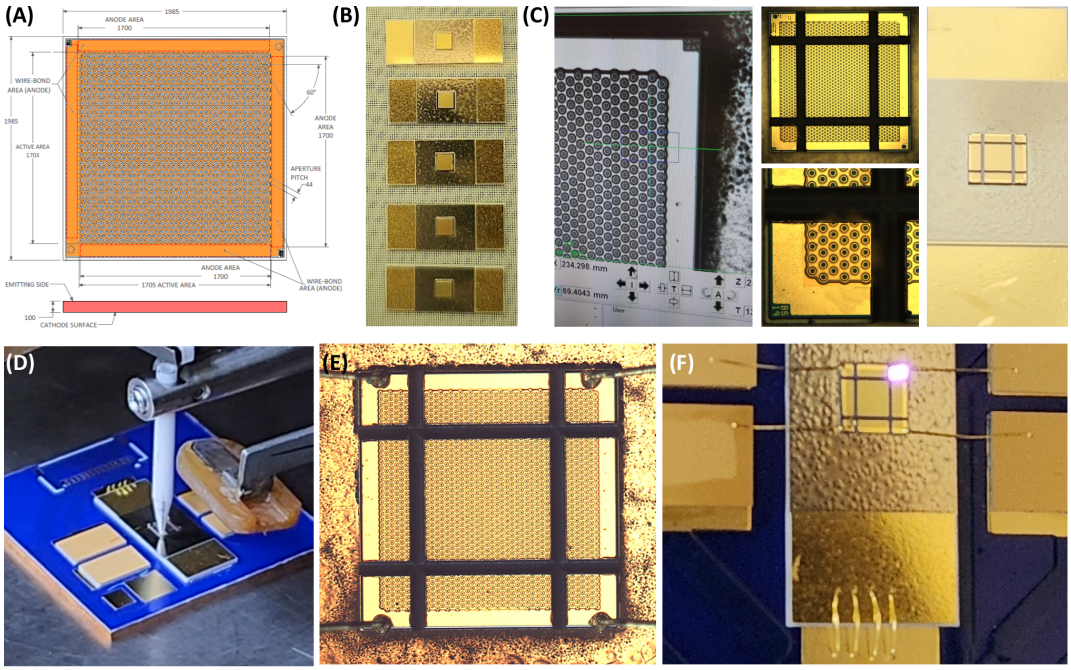

Figure 6. VCSEL chip preparation for printing: (A) VIXAR MM-VCSEL chip layout and dimensions; (B) VCSEL chip soldered onto BeO submount; (C) 50 μm deep dicing streets applied to singulate corner elements; (D) Wire bonding corner elements to contact pads on PCB; (E) VCSEL chip with wire bonds at corner regions; (F) Packaged chip allowing independent operation of VCSELs in each corner.

References

1. Maeda, T. *et al.* Mode conversion based on dual-phase modulation utilizing interference of two-phase-modulated beams. *Opt. Rev.* **25**, 734–742 (2018).
2. Shibukawa, A., Okamoto, A., Goto, Y., Honma, S. & Tomita, A. Digital phase conjugate mirror by parallel arrangement of two phase-only spatial light modulators. *Opt. Express* **22**, 11918–11929, DOI: 10.1364/OE.22.011918 (2014).
3. Zhang, Y. & Fontaine, N. K. Multi-plane light conversion: A practical tutorial (2023). 2304.11323.
4. Peng, Y., Choi, S., Padmanaban, N. & Wetzstein, G. Neural holography with camera-in-the-loop training. *ACM Transactions on Graph. (TOG)* **39**, 1–14 (2020).
5. Khare, K., Lochab, P. & Senthilkumaran, P. *Orbital angular momentum states of light: propagation through atmospheric turbulence* (IOP Publishing, 2024).